

Gated Differential Linear Attention: A Linear-Time Decoder for High-Fidelity Medical Segmentation

Hongbo Zheng¹ Afshin Bozorgpour² Dorit Merhof² Minjia Zhang¹
University of Illinois Urbana-Champaign¹ University of Regensburg²

Abstract

Medical image segmentation requires models that preserve fine anatomical boundaries while remaining efficient for clinical deployment. While transformers capture long-range dependencies, they suffer from quadratic attention cost and large data requirements, whereas CNNs are compute-friendly yet struggle with global reasoning. Linear attention offers $\mathcal{O}(N)$ scaling, but often exhibits training instability and attention dilution, yielding diffuse maps. We introduce PVT-GDLA, a decoder-centric Transformer that restores sharp, long-range dependencies at linear time. Its core, Gated Differential Linear Attention (GDLA), computes two kernelized attention paths on complementary query/key subspaces and subtracts them with a learnable, channel-wise scale to cancel common-mode noise and amplify relevant context. A lightweight, head-specific gate injects nonlinearity and input-adaptive sparsity, mitigating attention sink, and a parallel local token-mixing branch with depthwise convolution strengthens neighboring-token interactions, improving boundary fidelity, all while retaining $\mathcal{O}(N)$ complexity and low parameter overhead. Coupled with a pretrained Pyramid Vision Transformer (PVT) encoder, PVT-GDLA achieves state-of-the-art accuracy across CT, MRI, ultrasound, and dermoscopy benchmarks under equal training budgets, with comparable parameters but lower FLOPs than CNN-, Transformer-, hybrid-, and linear-attention baselines. PVT-GDLA provides a practical path to fast, scalable, high-fidelity medical segmentation in clinical environments and other resource-constrained settings.

1. Introduction

Medical image segmentation is fundamental to screening, diagnosis, and intervention planning in radiology, ultrasound, and dermatology. Reliable systems must combine *global context* to reason over distant structures, with *fine boundary fidelity* for small or thin anatomies, all under tight compute budgets typical of clinical environments. Balancing these requirements remains challenging: convolutional

neural networks (CNNs) [16, 23, 31] offer locality and efficiency but struggle with long-range dependencies, while Transformer backbones [7, 8, 10, 26] capture global relations at the cost of quadratic attention and elevated data and compute demands.

Linear attention reduces the memory and time of attention from $\mathcal{O}(N^2)$ to $\mathcal{O}(N)$ by replacing softmax with kernel feature maps and exploiting associativity [6, 14, 18, 34, 35]. However, its nonnegative, approximately linear similarity can over-smooth context, yielding diffuse, low-contrast attention that blurs boundaries (*attention dilution*) [27]. In recent work, *differential attention* was introduced to subtract complementary attention maps to cancel common-mode noise and sharpen focus [42], and *lightweight gating* injects beneficial nonlinearity and input-adaptive sparsity for stability [28].

In order to further improve the performance of linear-attention while maintaining the $\mathcal{O}(N)$ complexity, we propose a decoder-centric architecture built around *Gated Differential Linear Attention* (GDLA). GDLA computes two kernelized attention outputs on complementary query/key subspaces and subtracts them with a learnable, channel-wise scale to amplify relevant context while suppressing noise, without abandoning linear-time complexity. A head-specific gate introduces nonlinearity and query-dependent sparsity, mitigating attention sink with negligible parameter overhead. To strengthen short-range interactions, a depthwise convolutional local mixer augments the attention paths. We pair this decoder with a strong pretrained encoder, the Pyramid Vision Transformer (PVT) [40], yielding a simple, yet powerful PVT-GDLA design. Our novel model design achieves state-of-the-art performance across CT, MRI, ultrasound, and dermoscopy benchmarks at comparable parameter counts, but lower FLOPs than CNN-, Transformer-, hybrid-, and linear-attention baselines.

Our contributions are as follows:

- **Gated Differential Linear Attention.** We introduce a subtraction operator between two kernelized attention paths that suppresses common-mode responses and sharpens focus while retaining $\mathcal{O}(N)$ scaling. A head-specific gate adds nonlinearity and input-adaptive sparsity

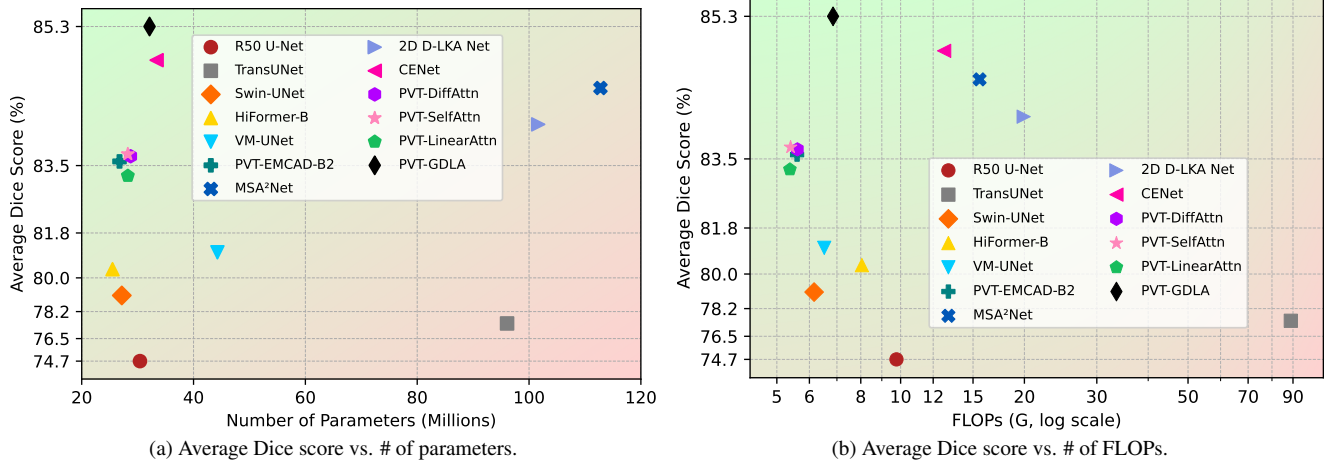


Figure 1. Comparison of model performance on Synapse dataset and compute-accuracy trade-off. Our approach achieves the highest Dice score with lower # parameters and lower # FLOPs.

with minimal overhead, improving stability and accuracy.

- **Local Token Mixing.** A lightweight depth-wise-pointwise convolutional branch enhances neighboring-token interactions, improving boundary fidelity and complementing the global receptive field of linear attention.
- **Strong accuracy-efficiency trade-off.** Under equal training budgets, PVT-GDLA achieves state-of-the-art results with comparable parameters, but lower computational cost across diverse modalities and datasets (Figure 1).

2. Related Works

2.1. Medical Segmentation Backbones

CNN backbones. U-shaped CNN networks remain highly competitive for medical segmentation due to their robust locality, translation equivariance, and efficient skip-connected decoding [9, 16, 23, 31]. Numerous refinements have been developed to enhance multi-scale fusion and boundary recovery, such as incorporating attention mechanisms or context modules in the decoder, while maintaining a favorable computational profile [26, 38]. These refinements include adapting deformable convolutions [3], dilated convolutions [13], and integrating attention mechanisms [26] to better represent high-level semantic feature maps. However, purely convolutional architectures may struggle to model long-range dependencies, which are essential for generating globally coherent predictions in complex anatomies.

Transformer and hybrid backbones. Transformer-based encoders and decoders have significantly advanced medical segmentation by facilitating global context aggregation [7, 8, 10]. However, the quadratic nature of

attention mechanisms increases memory and computational requirements, often necessitating larger datasets. CNN-Transformer hybrids seek to balance the advantages of locality and global interactions [8, 17]. Despite these advancements in hybrid frameworks, their dependence on global representations and fixed receptive fields can limit the accuracy of segmentation for varied structures across different scales.

2.2. Efficient (Kernelized) Attention

Quadratic self-attention is powerful but costly at high resolution. Kernelized/linear attention replaces softmax with nonnegative feature maps and exploits associativity to reduce time and memory from $\mathcal{O}(N^2)$ to $\mathcal{O}(N)$ [6, 14, 18, 34, 35]. Despite this efficiency, nonnegative kernels can induce *attention dilution*, over-smoothing that weakens boundaries and fine structures [27]. Quadratic self-attention is powerful but costly at high resolution. Kernelized/linear attention replaces softmax with nonnegative feature maps and exploits associativity to reduce time and memory from $\mathcal{O}(N^2)$ to $\mathcal{O}(N)$ [6, 14, 18, 34, 35]. Despite this efficiency, nonnegative kernels can induce *attention dilution*, over-smoothing that weakens boundaries and fine structures [27].

2.3. Gating Mechanisms in Attention and FFNs

The gating mechanism facilitates input-adaptive sparsity and context-aware semantic representation, enhancing feature representation through nonlinearity. This approach enables the selective enhancement of relevant features [12] while suppressing irrelevant ones [5], promoting adaptivity and stability [21], and mitigating attention sinks with minimal computational overhead [28, 33]. In practice, post-attention gates (value-path gates) or gated feedforward networks (FFNs) tend to improve boundary detail, multi-scale representation, and calibration in dense computer vision

tasks, such as medical image segmentation, where highly detailed feature representation is crucial.

2.4. Decoder Design for Medical Segmentation

Recent decoders emphasize multi-scale fusion and boundary-aware refinement, often combining attention with lightweight convolutions to recover fine detail at low FLOPs/params [5, 10, 30]. Specifically, CENet [5] augments skip connections with gated/context modules and denoising to enhance boundary fidelity across radiology and dermoscopy. Additionally, EMCAD [30] provides an efficient decoding module with multi-scale convolutional decoder, convolutional attention module, and large-kernel grouped attention gate. However, these architectures still mainly focus on convolutional modules and suffer from capturing long-range information.

3. Methodology

We present a decoder-centric hybrid architecture that pairs a pretrained Pyramid Vision Transformer (PVT) encoder with a *Gated Differential Linear Attention* (GDLA) decoder. GDLA retains the linear-time complexity of linear attention with respect to the number of tokens N , i.e., $\mathcal{O}(N)$, while (i) sharpening attention via a differential refinement (Section 3.2.1), (ii) increasing the expressiveness of the low-rank attention mapping through a lightweight, input-dependent gate (Section 3.2.1) and (iii) enriching neighboring token context by a parallel local token-mixing branch (Section 3.3). An overview of the architecture is shown in Figure 2.

3.1. Preliminaries

3.1.1. Multi-Head Differential Attention

Differential attention [42] sharpens focus by subtracting two attention maps computed over complementary subspaces. Compared to standard softmax attention [37], which forms a *single* attention map $\text{softmax}(\mathbf{Q}\mathbf{K}^\top/\sqrt{d_k})$ and applies it to \mathbf{V} , differential attention first splits queries/keys into two complementary channel subspaces, builds *two* attention maps, and combines them via a learnable subtraction.

Input Linear Projections. Given a tokenized input $\mathbf{X} \in \mathbb{R}^{N \times d_{\text{model}}}$, we form two query/key subspaces by first projecting to a total width d_k and then splitting channels:

$$[\mathbf{Q}_1; \mathbf{Q}_2] = \mathbf{X}\mathbf{W}^Q, [\mathbf{K}_1; \mathbf{K}_2] = \mathbf{X}\mathbf{W}^K, \mathbf{V} = \mathbf{X}\mathbf{W}^V \quad (1)$$

with $\mathbf{W}^Q, \mathbf{W}^K$, and $\mathbf{W}^V \in \mathbb{R}^{d_{\text{model}} \times d_k}$. Here, $\mathbf{Q}_1, \mathbf{Q}_2, \mathbf{K}_1, \mathbf{K}_2 \in \mathbb{R}^{N \times d_k/2}$ and $\mathbf{V} \in \mathbb{R}^{N \times d_k}$.

Differential Attention. Let $\lambda \in \mathbb{R}$ be a learnable scalar. Define two softmax attention map as

$$\mathbf{A}_1 = \text{softmax}\left(\frac{\mathbf{Q}_1\mathbf{K}_1^\top}{\sqrt{d_k/2}}\right) \quad \mathbf{A}_2 = \text{softmax}\left(\frac{\mathbf{Q}_2\mathbf{K}_2^\top}{\sqrt{d_k/2}}\right) \quad (2)$$

and the differential attention output

$$\text{DiffAttn}(\mathbf{Q}, \mathbf{K}, \mathbf{V}, \lambda) = (\mathbf{A}_1 - \lambda\mathbf{A}_2)\mathbf{V} \quad (3)$$

To synchronize the learning dynamics of the two subspaces, λ is re-parameterized as

$$\lambda = \exp(\boldsymbol{\lambda}_{q_1}\boldsymbol{\lambda}_{k_1}) - \exp(\boldsymbol{\lambda}_{q_2}\boldsymbol{\lambda}_{k_2}) + \lambda_{\text{init}}, \quad (4)$$

where $\boldsymbol{\lambda}_{q_1}, \boldsymbol{\lambda}_{k_1}, \boldsymbol{\lambda}_{q_2}, \boldsymbol{\lambda}_{k_2} \in \mathbb{R}^{d_k/2}$ are learnable vectors. The initialization

$$\lambda_{\text{init}} = 0.8 - 0.6 \times \exp(-0.3(l-1)) \quad (5)$$

works well empirically, where $l \in \{1, \dots, L\}$ indexes the layer.

Multi-Head Concatenation. Multi-head differential attention mirrors the standard multi-head formulation. With per-head projections $\mathbf{W}_i^Q, \mathbf{W}_i^K, \mathbf{W}_i^V \in \mathbb{R}^{d_{\text{model}} \times d_h}$, and a *layer-shared* scalar λ , each head is

$$\text{head}_i = \text{DiffAttn}(\mathbf{Q}\mathbf{W}_i^Q, \mathbf{K}\mathbf{W}_i^K, \mathbf{V}\mathbf{W}_i^V, \lambda). \quad (6)$$

To improve the gradient statistics, RMSNorm and a fixed rescaling are applied

$$\text{head}'_i = (1 - \lambda_{\text{init}}) \cdot \text{RMSNorm}(\text{head}_i). \quad (7)$$

Concatenating across heads yields

$$\text{MultiHead}(\mathbf{Q}, \mathbf{K}, \mathbf{V}, \lambda) = \text{Concat}(\text{head}'_1, \dots, \text{head}'_h). \quad (8)$$

Final Output Projection. The concatenated output is projected with $\mathbf{W}^O \in \mathbb{R}^{hd_h \times d_{\text{model}}}$ as in standard multi-head attention.

Final Output Projection. The output goes through the same process as the multi-head softmax attention.

3.1.2. Kernalized (Linear) Attention

Standard multi-head softmax attention incurs quadratic complexity $\mathcal{O}(N^2)$ in the sequence length N . Linear attention [18] reduces this to $\mathcal{O}(N)$. Its input projections, multi-head concatenation, and final output projection mirror those of multi-head softmax attention.

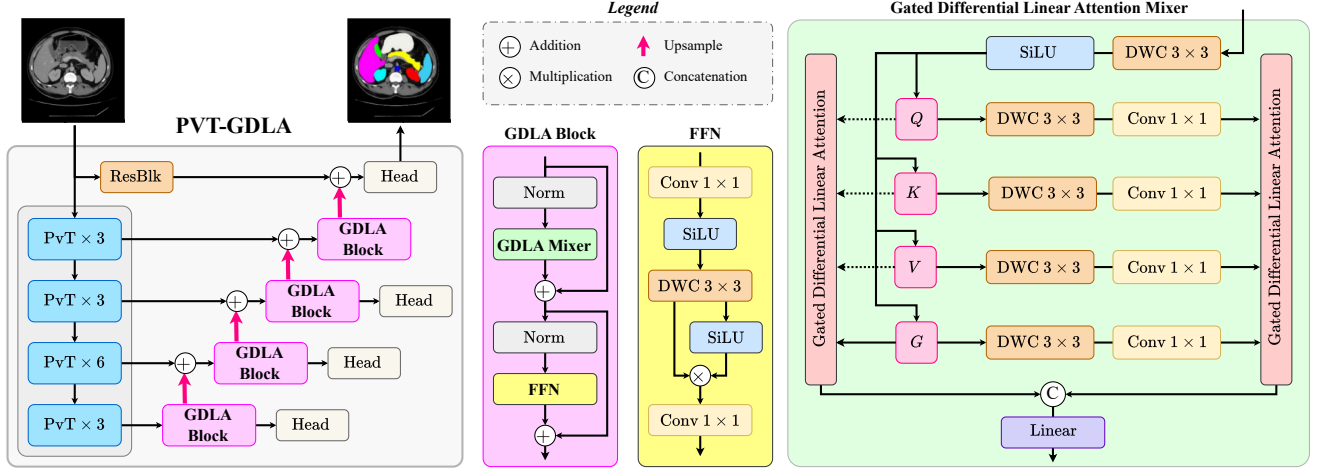


Figure 2. PVT-GDLA overview. A pretrained Pyramid Vision Transformer (PVT) encoder produces multi-scale features that feed a decoder built from GDLA blocks, which incorporates a GDLA mixer and a FFN. In each GDLA mixer, queries/keys are split into complementary subspaces; each branch performs gated differential kernelized linear attention. A parallel local token-mixing branch (depthwise 3×3 followed by 1×1) reinforces neighborhood interactions; fused outputs are projected and upsampled with skip connections to recover spatial resolution. Positional embedding is replaced with a 3×3 depth-wise convolution (DWC). Deep-supervision [20] is employed to improve the convergence speed.

Linear Attention. To avoid the quadratic cost of softmax attention, linear attention replaces the softmax similarity with a nonnegative feature map

$$\phi : \mathbb{R}^{d_k} \rightarrow \mathbb{R}_{\geq 0}^{d_k} \quad (9)$$

so that the similarity becomes

$$\langle \mathbf{Q}, \mathbf{K} \rangle_\phi = \phi(\mathbf{Q})\phi(\mathbf{K})^\top. \quad (10)$$

The normalized linear attention output is

$$\text{LinearAttn}(\mathbf{Q}, \mathbf{K}, \mathbf{V}) = [\phi(\mathbf{Q})\phi(\mathbf{K})^\top] \mathbf{V} \oslash \mathbf{z}, \quad (11)$$

where \oslash denotes element-wise division (broadcast across channels) and

$$\mathbf{z} = \phi(\mathbf{Q})[\phi(\mathbf{K})^\top \mathbf{1}_n] \in \mathbb{R}^n, \quad (12)$$

is the normalization vector, ensuring that each row sums appropriately. Using associativity, the computation can be reordered to achieve linear time:

$$\text{LinearAttn} = \phi(\mathbf{Q})[\phi(\mathbf{K})^\top \mathbf{V}] \oslash \mathbf{z}. \quad (13)$$

3.2. Gated Differential Linear Attention Mixer

We introduce a *Gated Differential Linear Attention (GDLA) mixer*, an enhanced variant of linear attention that preserves $\mathcal{O}(N)$ time complexity while improving accuracy and reducing computation.

3.2.1. Gated Differential Linear Attention

While linear attention efficiently captures long-range context, its strictly nonnegative kernel features bias it toward low-pass mixing, leading to *attention dilution* [27]. We therefore integrate the differential attention mechanism [42] into the linear-attention module: two attention maps are computed on complementary subspaces of \mathbf{Q} and \mathbf{K} with a shared \mathbf{V} and then subtracted.

Input Linear Projections. Given tokenized input $\mathbf{X} \in \mathbb{R}^{N \times d_{\text{model}}}$, we project into two query/key subspaces:

$$[\mathbf{Q}_1; \mathbf{Q}_2] = \mathbf{X} \mathbf{W}^Q, \quad [\mathbf{K}_1; \mathbf{K}_2] = \mathbf{X} \mathbf{W}^K, \quad \mathbf{V} = \mathbf{X} \mathbf{W}^V \quad (14)$$

with \mathbf{W}^Q , \mathbf{W}^K , and $\mathbf{W}^V \in \mathbb{R}^{d_{\text{model}} \times d_k}$. Here, \mathbf{Q}_1 , \mathbf{Q}_2 , \mathbf{K}_1 , $\mathbf{K}_2 \in \mathbb{R}^{N \times d_k/2}$ and $\mathbf{V} \in \mathbb{R}^{N \times d_k}$.

Differential Linear Attention. To retain $\mathcal{O}(N)$ complexity, linear attention computes $\phi(\mathbf{K})^\top \mathbf{V}$ before mixing with $\phi(\mathbf{Q})$. Hence, the two branches must be evaluated separately (rather than subtracting attention maps prior to applying \mathbf{V}). Let $\phi : \mathbb{R}^{d_k} \rightarrow \mathbb{R}_{\geq 0}^{d_k}$ be the feature map used in kernelized attention (we use $\phi(\cdot) = \text{ELU} + 1$ in our design). We form

$$\mathbf{A}_1 = \phi(\mathbf{Q}_1)[\phi(\mathbf{K}_1)^\top \mathbf{V}] \oslash \mathbf{z}_1 \quad (15)$$

$$\mathbf{A}_2 = \phi(\mathbf{Q}_2)[\phi(\mathbf{K}_2)^\top \mathbf{V}] \oslash \mathbf{z}_2, \quad (16)$$

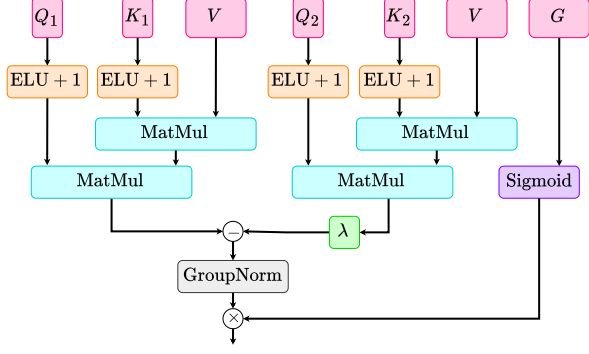


Figure 3. Gated Differential Linear Attention (GDLA). Two complementary query/key subspaces $\mathbf{Q}_1, \mathbf{K}_1$ and $\mathbf{Q}_2, \mathbf{K}_2$ are formed from \mathbf{X} . Each branch computes kernelized linear attention in $\mathcal{O}(N)$ by first contracting $\phi(\mathbf{K}_i)^\top \mathbf{V}$, then mixing with $\phi(\mathbf{Q}_i)$ and normalizing by \mathbf{z}_i . We use $\phi(\cdot) = \text{ELU} + 1$ as the kernel function to ensure non-negativity in attention scores. The outputs are combined via a learnable, channel-wise subtraction $\mathbf{A}_1 - \mathbf{A}_2 \odot \boldsymbol{\lambda}$, stabilized with RMSNorm, and modulated by a data-dependent Sigmoid gate $\mathbf{G}_i = \sigma(\mathbf{X}\mathbf{W}_i^G)$.

where \odot denotes element-wise division (broadcast across channels), and

$$\mathbf{z}_i = \phi(\mathbf{Q}_i)[\phi(\mathbf{K}_i)^\top \mathbf{1}_n], \quad i \in \{1, 2\} \quad (17)$$

Unlike softmax-based differential attention, no reparameterization of the subtraction coefficient is required here. We use a learnable vector $\boldsymbol{\lambda} \in \mathbb{R}^{d_k}$ to control the subtraction strength

$$\text{DiffLinearAttn}(\mathbf{Q}, \mathbf{K}, \mathbf{V}, \boldsymbol{\lambda}) = \mathbf{A}_1 - \boldsymbol{\lambda} \odot \mathbf{A}_2, \quad (18)$$

where \odot denotes the Hadamard product (channel-wise scaling).

Multi-Head Differential Linear Attention. As in standard attention, we compute the above in parallel for h heads with per-head projections $\mathbf{W}_i^Q, \mathbf{W}_i^K, \mathbf{W}_i^V \in \mathbb{R}^{d_{\text{model}} \times d_h}$ and a per-head subtraction vector $\boldsymbol{\lambda}_i \in \mathbb{R}^{d_h}, i \in \{1, \dots, h\}$. Let

$$\mathbf{Y}_i = \text{DiffLinearAttn}(\mathbf{Q}\mathbf{W}_i^Q, \mathbf{K}\mathbf{W}_i^K, \mathbf{V}\mathbf{W}_i^V, \boldsymbol{\lambda}_i). \quad (19)$$

We then stabilize gradients via RMS normalization

$$\hat{\mathbf{Y}}_i = \text{RMSNorm}(\mathbf{Y}_i). \quad (20)$$

Gating Mechanism. Kernelized attention is a linear, low-rank mapping; introducing a gate adds nonlinearity and promotes sparsity, which improves stability and mitigates attention sinks [28]. Empirically, a Sigmoid gate performs

better than SiLU for this role. Thus, we form a data-dependent gate $\mathbf{G}_i = \sigma(\mathbf{X}\mathbf{W}_i^G) \in \mathbb{R}^{N \times d_h}$, with $\mathbf{W}_i^G \in \mathbb{R}^{d_{\text{model}} \times d_h}$ and σ the sigmoid for each head. The gated per-head output is

$$\text{head}_i = \hat{\mathbf{Y}}_i \odot \mathbf{G}_i = \hat{\mathbf{Y}}_i \odot \sigma(\mathbf{X}\mathbf{W}_i^G) \in \mathbb{R}^{N \times d_h}. \quad (21)$$

Multi-Head Concatenation. Finally, we concatenate the head outputs along the channel dimension:

$$\text{MultiHead}(\mathbf{Q}, \mathbf{K}, \mathbf{V}, \boldsymbol{\lambda}, \mathbf{G}) = \text{Concat}(\text{head}_1, \dots, \text{head}_h). \quad (22)$$

3.3. Local Token Mixing Branch

Linear attention may suffer from *attention dilution*, where scores are spread too uniformly across the sequence, weakening preservation of salient local structure [27]. To reinforce short-range interactions, we add a parallel *local token-mixing* branch that augments the inputs to GDLA. Concretely, for each of $\mathbf{Q}, \mathbf{K}, \mathbf{V}, \mathbf{G}$ we apply a depthwise convolution (DWC) to mix information among neighboring tokens, followed by a pointwise convolution (PWC) to fuse channels [6]. This depthwise–pointwise sequence (i) captures spatial locality and (ii) preserves efficiency.

Let f denote the local mixer,

$$f(\cdot) = \text{Conv}_{1 \times 1}(\text{DWC}_{3 \times 3}(\cdot)), \quad (23)$$

applied on the token grid (for 2D inputs, tokens are reshaped to $\mathcal{H} \times \mathcal{W}$ and then mapped back to length $N = \mathcal{H}\mathcal{W}$).

Given input $\mathbf{X} \in \mathbb{R}^{N \times d_{\text{model}}}$ and learned projections $\mathbf{W}^Q, \mathbf{W}^K, \mathbf{W}^V, \mathbf{W}^G \in \mathbb{R}^{d_{\text{model}} \times d_k}$, we form the locally mixed inputs (splitting queries/keys into complementary subspaces as in GDLA):

$$[\mathbf{Q}'_1; \mathbf{Q}'_2] = f(\mathbf{X}\mathbf{W}^Q) \quad [\mathbf{K}'_1; \mathbf{K}'_2] = f(\mathbf{X}\mathbf{W}^K) \quad (24)$$

$$\mathbf{V}' = f(\mathbf{X}\mathbf{W}^V) \quad \mathbf{G}' = f(\mathbf{X}\mathbf{W}^G), \quad (25)$$

where $\mathbf{Q}'_1, \mathbf{Q}'_2, \mathbf{K}'_1, \mathbf{K}'_2, \mathbf{V}', \mathbf{G}' \in \mathbb{R}^{N \times d_k}$. The subsequent multi-head computation and gating follow GDLA verbatim, substituting the primed tensors for their unprimed counterparts.

3.4. Output Fusion

We fuse the outputs of the global (GDLA) and local token-mixing branches with a final linear projection. Let σ denote the element-wise Sigmoid and \odot the Hadamard product (broadcast across channels). With $\mathbf{W}^O \in \mathbb{R}^{2d_{\text{model}} \times d_{\text{model}}}$,

$$\hat{\mathbf{Y}} = \text{MultiHead}(\mathbf{Q}, \mathbf{K}, \mathbf{V}, \boldsymbol{\lambda}, \mathbf{G}) \quad (26)$$

$$\hat{\mathbf{Y}}' = \text{MultiHead}(\mathbf{Q}', \mathbf{K}', \mathbf{V}', \boldsymbol{\lambda}', \mathbf{G}') \quad (27)$$

$$\mathbf{O} = \text{Concat}(\hat{\mathbf{Y}}, \hat{\mathbf{Y}}')\mathbf{W}^O \in \mathbb{R}^{N \times d_{\text{model}}} \quad (28)$$

This fusion preserves $\mathcal{O}(N)$ complexity while combining long-range context from GDLA with enhanced local interactions, improving robustness to attention dilution.

Table 1. Evaluation results on the Synapse dataset (blue indicates the best and red the second best results). Results are averaged over three runs.

Methods	Params	FLOPs	Spl.	RKid.	LKid.	Gal.	Liv.	Sto.	Aor.	Pan.	Average	
											DSC \uparrow	HD95 \downarrow
R50+U-Net [8]	30.42 M	-	85.87	78.19	80.60	63.66	93.74	74.16	87.74	56.90	74.68	36.87
TransUNet [8]	96.07 M	88.91 G	85.08	77.02	81.87	63.16	94.08	75.62	87.23	55.86	77.49	31.69
Swin-UNet [7]	27.17 M	6.16 G	90.66	79.61	83.28	66.53	94.29	76.60	85.47	56.58	79.13	21.55
HiFormer-B [15]	25.51 M	8.05 G	90.99	79.77	85.23	65.23	94.61	81.08	86.21	59.52	80.39	14.70
VM-UNet [32]	44.27 M	6.52 G	89.51	82.76	86.16	69.41	94.17	81.40	86.40	58.80	81.08	19.21
PVT-EMCAD-B2 [30]	26.76 M	5.60 G	92.17	84.10	88.08	68.87	95.26	83.92	88.14	68.51	83.63	15.68
MSA ² Net [19]	112.77 M	15.56 G	92.69	84.24	88.30	74.35	95.59	84.03	89.47	69.30	84.75	13.29
2D D-LKA Net [3]	101.64 M	19.92 G	91.22	84.92	88.38	73.79	94.88	84.94	88.34	67.71	84.27	20.04
CENet [5]	33.39 M	12.76 G	93.58	85.08	91.18	68.29	95.92	81.68	89.19	70.71	85.04	8.84
PVT-DiffAttn [42]	28.75 M	5.61 G	92.17	83.43	86.94	68.64	95.73	85.74	88.28	68.94	83.73	23.24
PVT-SelfAttn [37]	28.25 M	5.40 G	91.72	85.67	87.20	67.88	95.92	85.00	89.79	66.93	83.77	22.40
PVT-LinearAttn [18]	28.25 M	5.38 G	90.46	83.22	87.02	69.00	95.92	85.54	88.23	67.28	83.33	18.62
PVT-GDLA	32.13 M	6.85 G	92.96	85.03	90.16	69.97	96.32	88.99	88.26	70.86	85.32	12.41

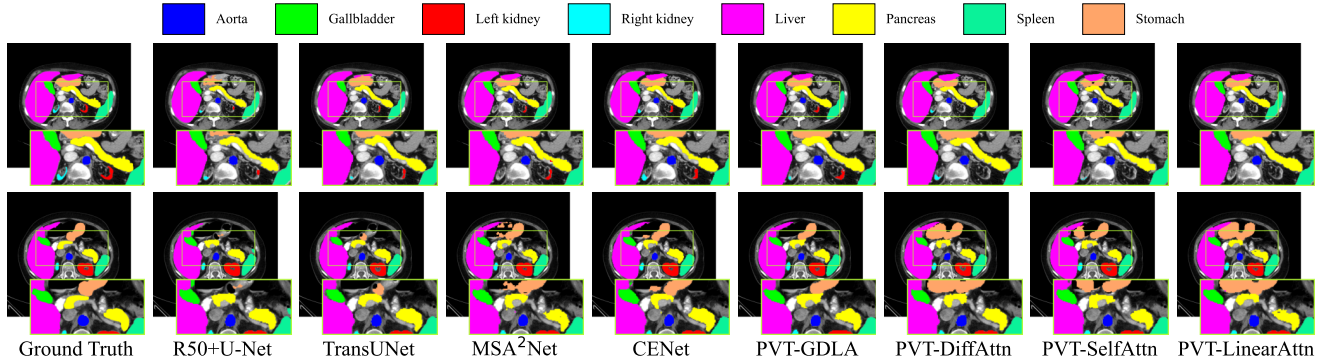


Figure 4. Qualitative results of the proposed method versus other approaches on the *Synapse* dataset.

3.5. Feed-Forward Network

We evaluate several FFN designs: (i) the classic two-layer MLP with $4\times$ expansion [37], (ii) SwiGLU [33], a $4\times$ -expanded two-layer MLP with an additional mid-layer gate as in modern Large Language Models (LLMs), and (iii) a SwiGLU-style Mix-FFN that replaces the gate with a depthwise $k\times k$ convolution (DWC) to capture local structure [41]. Empirically, Mix-FFN works best with our novel GDLA because the DWC provides extra token mixing among neighbors, and the SiLU nonlinearity enhances expressiveness and stability.

Let $\mathbf{X} \in \mathbb{R}^{N \times d_{\text{model}}}$ be the input and $d_{\text{hidden}} = \alpha d_{\text{model}}$ (we use $\alpha=4$ unless noted). Mix-FFN is:

$$[\hat{\mathbf{X}}; \mathbf{G}] = \text{DWC}_{3 \times 3}(\text{SiLU}(\text{Conv}_{1 \times 1}(\mathbf{X}))) \in \mathbb{R}^{N \times 2d_{\text{hidden}}} \quad (29)$$

$$\mathbf{Y} = \text{Conv}_{1 \times 1}(\hat{\mathbf{X}} \odot \text{SiLU}(\mathbf{G})) \in \mathbb{R}^{N \times d_{\text{model}}}, \quad (30)$$

where \odot denotes the Hadamard (element-wise) product. We use $k=3$ in our main experiments; larger k values are possible with a modest cost increase.

4. Experiment

We first detail the implementation and datasets used to evaluate PVT-GDLA. Performance is assessed across multiple datasets spanning different imaging modalities, such as CT, MRI, ultrasound, and dermoscopy. Our model is implemented in PyTorch, trained on an NVIDIA L40S GPU (46 GB) with input resolution 224×224 , and utilizes the BDoU loss [29].

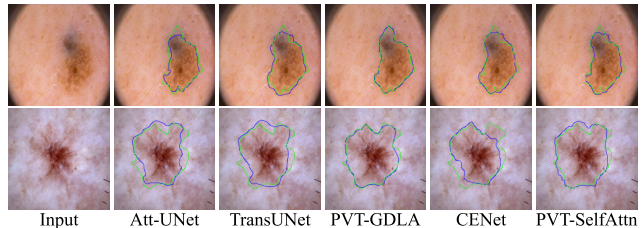


Figure 5. Visual comparison of the proposed method versus others on the Skin datasets. PH^2 (top) and $HAM10000$ (bottom). The blue and the green lines represent prediction and ground truth respectively.

Table 2. Evaluation results on the ACDC (left), BUSI (middle), and skin-lesion benchmarks PH^2 and HAM10000 (right). All metrics are averaged over three runs.

Methods	Avg. Dice	RV	MYO	LV	Methods	Avg. Dice	PH ²		HAM10000		
							Dice	Acc.	Dice	Acc.	
R50+UNet [8]	87.55	87.10	80.63	94.92	U-Net [31]	74.04	89.36	92.33	91.67	95.67	
R50+AttnUNet [8]	86.75	87.58	79.20	93.47	PraNet [11]	75.41	88.40	92.00	93.53	96.49	
TransUNet [8]	89.71	88.86	84.53	95.73	CaraNet [24]	77.34	94.49	96.78	92.63	96.16	
Swin-UNet [7]	90.00	88.55	85.62	95.83	AttnUNet [26]	74.48	92.02	95.03	92.51	96.07	
R50+ViT+CUP [8]	87.57	86.07	81.88	94.75	DeepLabv3+ [2]	76.81	90.03	92.76	92.68	96.10	
MT-UNet [39]	90.43	86.64	89.04	95.62	TransUNet [8]	78.30	90.93	94.08	93.46	96.84	
MISSFormer [17]	90.86	89.55	88.04	94.99	TransFuse [43]	79.36	85.50	90.50	92.11	96.21	
PVT-EMCAD-B2 [30]	92.12	90.65	89.68	96.02	Swin-UNet [7]	77.38	95.04	97.19	94.71	97.04	
CENet [5]	92.18	90.90	89.63	95.99	PVT-EMCAD-B2 [30]	80.25	PVT-DiffAttn [42]	95.10	97.13	94.73	97.10
PVT-DiffAttn [42]	92.20	90.64	89.90	96.06	PVT-DiffAttn [42]	79.84	PVT-SelfAttn [37]	95.08	97.18	94.78	97.06
PVT-SelfAttn [37]	92.10	90.47	89.76	96.06	PVT-SelfAttn [37]	79.42	PVT-LinearAttn [18]	94.78	96.68	94.68	96.87
PVT-LinearAttn [18]	91.77	89.80	89.52	96.00	PVT-LinearAttn [18]	79.14					
PVT-GDLA	92.53	91.30	90.21	96.07	PVT-GDLA	80.54	PVT-GDLA	95.59	97.20	95.01	97.38

4.1. Results

Radiology. The performance of PVT-GDLA on radiological datasets is evaluated, with Table 1 presenting the quantitative results on the Synapse CT dataset using Dice score and HD metrics, and Table 2 showing the quantitative results on the ACDC dataset [4]. Our approach outperforms existing CNN-based, Transformer-based, and hybrid models. PVT-GDLA achieves the SoTA performance with comparable number of parameters but lower FLOPs. These results underscore PVT-GDLA’s ability in segmenting various organs. Figure 4 provides a visual representation of PVT-GDLA’s performance in segmenting various organs, demonstrating PVT-GDLA’s accuracy in multi-scale segmentation of the liver, stomach, pancreas, spleen, and kidneys. Additionally, PVT-GDLA also shows effectiveness on the ACDC dataset for cardiac segmentation in the MRI image, achieves the highest average Dice score of 92.53%, and excels in all three organ segmentation tasks.

Ultrasound. We evaluate on the BUSI breast ultrasound dataset [1]. As summarized in Table 2, PVT-GDLA attains the best average Dice of 80.54% surpassing prior PVT-based baseline (PVT-EMCAD-B2) by +0.29% and outperforms other PVT decoders, PVT-DiffAttn, PVT-SelfAttn, and PVT-LinearAttn, by +0.70%, +1.12%, and +1.40% Dice, respectively.

Dermoscopy. Table 2 evaluates the proposed network on two skin lesion segmentation datasets, HAM10000 [36] and PH^2 [25] using Dice and accuracy metrics. PVT-GDLA outperforms CNN-based, Transformer-based, and hybrid methods, demonstrating superior performance and generalization. Moreover, Figure 5 showcases PVT-GDLA’s capability in capturing intricate structures and producing precise boundaries through effective boundary integration.

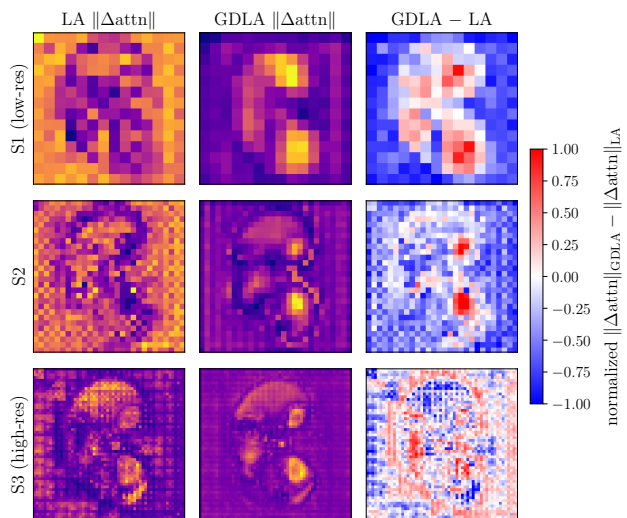


Figure 6. Linear Attention (LA) vs. Gated Differential Linear Attention (GDLA) on a Synapse CT slice. Rows correspond to decoder stages (coarse → fine); columns show token-norm maps $\|\text{input}\|$ and update magnitudes $\|\Delta\text{attn}\|$ for LA (left) and GDLA (right), with a difference panel visualizing normalized $\|\Delta\text{attn}\|$ (GDLA-LA). The input image and the ground truth segmentation is shown in Figure 7.

4.2. Attention Visualization

Across all decoder stages, the visualization in Figure 6 shows that linear attention (LA) produces highly diffused token activations and noisy attention maps, whereas gated differential linear attention (GDLA) yields sharper, anatomically coherent responses that align with organ structures in the Synapse CT slices. In the LA columns, the input norm maps $\|\text{input}\|$ already exhibit spatially smeared activations, and the corresponding $\|\Delta\text{attn}\|$ maps are dominated by high-frequency speckle, indicating that attention updates are largely unconstrained and mix information indiscriminately across the field of view. In contrast, GDLA’s input norms preserve clear silhouettes of organs at all decoder

levels, and its $\|\Delta\text{attn}\|$ maps are concentrated along organ interiors and boundaries with background regions strongly suppressed, mitigating attention dilution.

Figure 7 reports the Channel Saliency Map (CSM), which computes root-mean-square (RMS) feature energy per token for each decoder layer. Under LA, the *first token* exhibits disproportionately high energy relative to others, showcasing the problem of attention sink. Moreover, the foreground–background contrast is weak, illustrating the attention dilution issue. By comparison, GDLA avoids collapse onto a few positions (especially the first token) and maintains a balanced, structure-aware energy distribution, consistent with focused yet non-collapsing attention dynamics. These observations corroborate the qualitative trends in Figure 6.

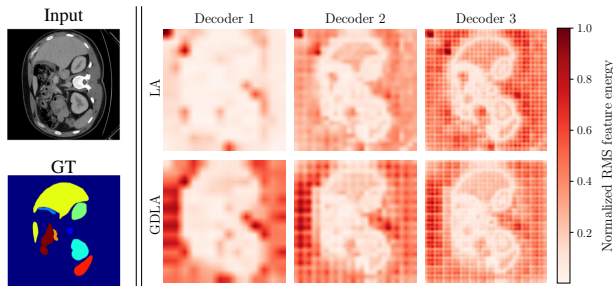


Figure 7. Channel saliency across decoder stages. Normalized RMS feature–energy per channel for Decoder 1–3 (coarse to fine) comparing linear attention (LA) and GDLA. The left column includes the input data and ground truth segmentation.

4.3. Ablation Study

Table 3. Effect of different components of PVT-GDLA on the PH^2 datasets. All results are averaged over three runs. The best result is shown in bold.

Components			Params	FLOPs	Dice
DiffAttn	Mixer	Gate			
✗	✗	✗	28.25 M	5.38 G	94.78
✓	✗	✗	29.89 M	6.05 G	95.08
✓	✗	✓	30.01 M	6.10 G	95.20
✓	✓	✗	31.13 M	6.52 G	95.46
✓	✓	✓	32.13 M	6.85 G	95.59

4.3.1. Effect of Different Components

We assess the contribution of PVT-GDLA’s components on PH^2 via controlled ablations against a linear-attention baseline. As summarized in Table 3, both DiffAttn and the local token-mixing branch yield the largest gains: adding DiffAttn improves the Dice score by $\approx 0.3\%$, while adding the mixer yields an additional $\approx 0.4\%$. Notably, DiffAttn

incurs smaller parameter and FLOPS overhead than the local mixer. Combined, they contribute $\approx 0.7\%$ Dice improvement over the linear-attention baseline. The Sigmoid gate provides a modest accuracy gain and, more importantly, stabilizes training. Overall, the full GDLA configuration achieves the best performance, improving Dice by $\approx 0.8\%$ over baseline.

Table 4. Effect of ConvTranspose kernel size in Upsample and depth-wise convolution kernel size in local token mixing on *Synapse* multi-organ, *ACDC*, *HAM10000* datasets. All results are averaged over three runs. Best results are highlighted in bold.

Kernel Size		Avg. Dice		
DWC	ConvTranspose	<i>Synapse</i>	<i>ACDC</i>	<i>HAM1000</i>
3×3	3×3	85.32	92.53	95.01
3×3	5×5	84.94	92.23	94.73
5×5	3×3	84.73	92.21	94.68
5×5	5×5	84.63	92.17	94.62

4.3.2. Effect of Kernel Size in Local Mixer and Upsample

Table 4 jointly varies the kernel sizes of DWC in the local token mixer and ConvTranspose in the upsampling layer on *Synapse*, *ACDC*, and *HAM10000*. The 3×3 – 3×3 setting achieves the best average Dice on all three datasets (85.32 / 92.53 / 95.01). Increasing either DWC or ConvTranspose to 5×5 yields consistent but modest degradations. We therefore adopt 3×3 kernels for both components by default.

5. Conclusion

The proposed PVT-GDLA improves the original linear attention by maintaining its efficiency and linear complexity while enhancing the context feature extraction by eliminating the attention noise in the linear attention caused by the attention dilution. PVT-GDLA’s superior accuracy and boundary preservation over SoTA methods is demonstrated on a broad range of medical datasets, highlighting that it provides a robust solution for complex segmentation tasks.

References

- [1] Walid Al-Dhabyani, Mohammed Gomaa, Hussien Khaled, and Aly Fahmy. Dataset of breast ultrasound images. *Data in brief*, 28:104863, 2020. 7, 1
- [2] Reza Azad, Maryam Asadi-Aghbolaghi, Mahmood Fathy, and Sergio Escalera. Attention deeplabv3+: Multi-level context attention mechanism for skin lesion segmentation. In *European conference on computer vision*, pages 251–266. Springer, 2020. 7
- [3] Reza Azad, Leon Niggemeier, Michael Huttemann, Amirhossein Kazerooni, Ehsan Khodapanah Aghdam, Yury

- Velichko, Ulas Bagci, and Dorit Merhof. Beyond self-attention: Deformable large kernel attention for medical image segmentation, 2023. 2, 6
- [4] Olivier Bernard, Alain Lalande, Clement Zotti, Frederick Cervenansky, Xin Yang, Pheng-Ann Heng, Irem Cetin, Karim Lekadir, Oscar Camara, Miguel Angel Gonzalez Ballester, et al. Deep learning techniques for automatic mri cardiac multi-structures segmentation and diagnosis: is the problem solved? *IEEE transactions on medical imaging*, 37(11):2514–2525, 2018. 7, 1
- [5] Afshin Bozorgpour, Sina Ghorbani Kolahi, Reza Azad, Ilker Hacihaliloglu, and Dorit Merhof. CENet: Context Enhancement Network for Medical Image Segmentation. In *proceedings of Medical Image Computing and Computer Assisted Intervention – MICCAI 2025*. Springer Nature Switzerland, 2025. 2, 3, 6, 7
- [6] Han Cai, Junyan Li, Muyan Hu, Chuang Gan, and Song Han. Efficientvit: Lightweight multi-scale attention for high-resolution dense prediction. In *Proceedings of the IEEE/CVF International Conference on Computer Vision (ICCV)*, pages 17302–17313, 2023. 1, 2, 5
- [7] Hu Cao, Yueyue Wang, Joy Chen, Dongsheng Jiang, Xiaopeng Zhang, Qi Tian, and Manning Wang. Swin-unet: Unet-like pure transformer for medical image segmentation. In *Proceedings of the European Conference on Computer Vision Workshops (ECCVW)*, 2022. 1, 2, 6, 7
- [8] Jieneng Chen, Yongyi Lu, Qihang Yu, Xiangde Luo, Ehsan Adeli, Yan Wang, Le Lu, Alan L Yuille, and Yuyin Zhou. Transunet: Transformers make strong encoders for medical image segmentation. *arXiv preprint arXiv:2102.04306*, 2021. 1, 2, 6, 7
- [9] Liang-Chieh Chen, Yukun Zhu, George Papandreou, Florian Schroff, and Hartwig Adam. Encoder-decoder with atrous separable convolution for semantic image segmentation. In *Proceedings of the European conference on computer vision (ECCV)*, pages 801–818, 2018. 2, 7
- [10] Bo Dong, Wenhai Wang, Deng-Ping Fan, Jinpeng Li, Huazhu Fu, and Ling Shao. Polyp-pvt: Polyp segmentation with pyramid vision transformers. *arXiv preprint arXiv:2108.06932*, 2021. 1, 2, 3
- [11] Deng-Ping Fan, Ge-Peng Ji, Tao Zhou, Geng Chen, Huazhu Fu, Jianbing Shen, and Ling Shao. Pranet: Parallel reverse attention network for polyp segmentation. In *International conference on medical image computing and computer-assisted intervention*, pages 263–273. Springer, 2020. 7
- [12] Mustansar Fiaz, Mubashir Noman, Hisham Cholakkal, Rao Muhammad Anwer, Jacob Hanna, and Fahad Shahbaz Khan. Guided-attention and gated-aggregation network for medical image segmentation. *Pattern Recognition*, 156: 110812, 2024. 2
- [13] Meng-Hao Guo, Cheng-Ze Lu, Zheng-Ning Liu, Ming-Ming Cheng, and Shi-Min Hu. Visual attention network. *Computational visual media*, 9(4):733–752, 2023. 2
- [14] Dongchen Han, Ziyi Wang, Zhuofan Xia, Yizeng Han, Yifan Pu, Chunjiang Ge, Jun Song, Shiji Song, Bo Zheng, and Gao Huang. Demystify mamba in vision: A linear attention perspective. *Advances in neural information processing systems*, 37:127181–127203, 2024. 1, 2
- [15] Moein Heidari, Amirhossein Kazerouni, Milad Soltany, Reza Azad, Ehsan Khodapanah Aghdam, Julien Cohen-Adad, and Dorit Merhof. Hiformer: Hierarchical multi-scale representations using transformers for medical image segmentation. In *Proceedings of the IEEE/CVF Winter Conference on Applications of Computer Vision*, pages 6202–6212, 2023. 6
- [16] Huimin Huang, Lanfen Lin, Ruofeng Tong, Hongjie Hu, Qiaowei Zhang, Yutaro Iwamoto, Xianhua Han, Yen-Wei Chen, and Jian Wu. Unet 3+: A full-scale connected unet for medical image segmentation. In *ICASSP 2020-2020 IEEE international conference on acoustics, speech and signal processing (ICASSP)*, pages 1055–1059. Ieee, 2020. 1, 2
- [17] Xiaohong Huang, Zhifang Deng, Dandan Li, Xueguang Yuan, and Ying Fu. Missformer: An effective transformer for 2d medical image segmentation. *IEEE Transactions on Medical Imaging*, 2022. 2, 7
- [18] Angelos Katharopoulos, Apoorv Vyas, Nikolaos Pappas, and François Fleuret. Transformers are RNNs: Fast autoregressive transformers with linear attention. In *Proceedings of the 37th International Conference on Machine Learning*, pages 5156–5165. PMLR, 2020. 1, 2, 3, 6, 7
- [19] Sina Ghorbani Kolahi, Seyed Kamal Chaharsooghi, Toktam Khatibi, Afshin Bozorgpour, Reza Azad, Moein Heidari, Ilker Hacihaliloglu, and Dorit Merhof. Msa²net: Multi-scale adaptive attention-guided network for medical image segmentation. *arXiv preprint arXiv:2407.21640*, 2024. 6
- [20] Chen-Yu Lee, Saining Xie, Patrick Gallagher, Zhengyou Zhang, and Zhuowen Tu. Deeply-Supervised Nets. In *Proceedings of the Eighteenth International Conference on Artificial Intelligence and Statistics*, pages 562–570, San Diego, California, USA, 2015. PMLR. 4
- [21] Siyuan Li, Zedong Wang, Zicheng Liu, Cheng Tan, Haitao Lin, Di Wu, Zhiyuan Chen, Jiangbin Zheng, and Stan Z Li. Moganet: Multi-order gated aggregation network. *arXiv preprint arXiv:2211.03295*, 2022. 2
- [22] Ilya Loshchilov and Frank Hutter. Decoupled weight decay regularization. In *International Conference on Learning Representations*, 2019. 1
- [23] Ange Lou, Shuyue Guan, and Murray Loew. Dc-unet: rethinking the u-net architecture with dual channel efficient cnn for medical image segmentation. In *Medical Imaging 2021: Image Processing*, pages 758–768. SPIE, 2021. 1, 2
- [24] Ange Lou, Shuyue Guan, Hanseok Ko, and Murray H Loew. Caranet: context axial reverse attention network for segmentation of small medical objects. In *Medical Imaging 2022: Image Processing*, pages 81–92. SPIE, 2022. 7
- [25] Teresa Mendonça, M Celebi, T Mendonca, and J Marques. Ph2: A public database for the analysis of dermoscopic images. *Dermoscopy image analysis*, 2, 2015. 7, 1
- [26] Ozan Oktay, Jo Schlemper, Loic Le Folgoc, Matthew Lee, Mattias Heinrich, Kazunari Misawa, Kensaku Mori, Steven McDonagh, Nils Y Hammerla, Bernhard Kainz, et al. Attention u-net: Learning where to look for the pancreas. *arXiv preprint arXiv:1804.03999*, 2018. 1, 2, 7
- [27] Zhen Qin, Xiaodong Han, Weixuan Sun, Dongxu Li, Lingpeng Kong, Nick Barnes, and Yiran Zhong. The devil in lin-

- ear transformer. In *Proceedings of the 2022 Conference on Empirical Methods in Natural Language Processing*, pages 7025–7041, Abu Dhabi, United Arab Emirates, 2022. Association for Computational Linguistics. 1, 2, 4, 5
- [28] Zihan Qiu, Zekun Wang, Bo Zheng, Zeyu Huang, Kaiyue Wen, Songlin Yang, Rui Men, Le Yu, Fei Huang, Suozhi Huang, et al. Gated attention for large language models: Non-linearity, sparsity, and attention-sink-free. *arXiv preprint arXiv:2505.06708*, 2025. 1, 2, 5
- [29] Md Mostafijur Rahman and Radu Marculescu. Multi-scale hierarchical vision transformer with cascaded attention decoding for medical image segmentation. In *Medical Imaging with Deep Learning (MIDL)*, 2023. 6
- [30] Md Mostafijur Rahman, Mustafa Munir, and Radu Marculescu. Emcad: Efficient multi-scale convolutional attention decoding for medical image segmentation. In *Proceedings of the IEEE/CVF Conference on Computer Vision and Pattern Recognition*, pages 11769–11779, 2024. 3, 6, 7
- [31] Olaf Ronneberger, Philipp Fischer, and Thomas Brox. U-net: Convolutional networks for biomedical image segmentation. In *International Conference on Medical image computing and computer-assisted intervention*, pages 234–241. Springer, 2015. 1, 2, 7
- [32] Jiacheng Ruan and Suncheng Xiang. Vm-unet: Vision mamba unet for medical image segmentation. *arXiv preprint arXiv:2402.02491*, 2024. 6
- [33] Noam Shazeer. Glu variants improve transformer. *arXiv preprint arXiv:2002.05202*, 2020. 2, 6
- [34] Zhuoran Shen, Mingyuan Zhang, Haiyu Zhao, Shuai Yi, and Hongsheng Li. Efficient attention: Attention with linear complexities. In *Proceedings of the IEEE/CVF winter conference on applications of computer vision*, pages 3531–3539, 2021. 1, 2
- [35] Yao-Hung Hubert Tsai, Shaojie Bai, Makoto Yamada, Louis-Philippe Morency, and Ruslan Salakhutdinov. Transformer dissection: a unified understanding of transformer’s attention via the lens of kernel. *arXiv preprint arXiv:1908.11775*, 2019. 1, 2
- [36] Philipp Tschandl, Cliff Rosendahl, and Harald Kittler. The ham10000 dataset, a large collection of multi-source dermatoscopic images of common pigmented skin lesions. *Scientific data*, 5(1):1–9, 2018. 7, 1
- [37] Ashish Vaswani, Noam Shazeer, Niki Parmar, Jakob Uszkoreit, Llion Jones, Aidan N Gomez, Łukasz Kaiser, and Illia Polosukhin. Attention is all you need. In *Advances in Neural Information Processing Systems*. Curran Associates, Inc., 2017. 3, 6, 7, 1
- [38] Haonan Wang, Peng Cao, Jiaqi Wang, and Osmar R Zaiane. Utransnet: rethinking the skip connections in u-net from a channel-wise perspective with transformer. In *Proceedings of the AAAI conference on artificial intelligence*, pages 2441–2449, 2022. 2, 7
- [39] Hongyi Wang, Shiao Xie, Lanfen Lin, Yutaro Iwamoto, Xian-Hua Han, Yen-Wei Chen, and Ruofeng Tong. Mixed transformer u-net for medical image segmentation. In *ICASSP 2022-2022 IEEE international conference on acoustics, speech and signal processing (ICASSP)*, pages 2390–2394. IEEE, 2022. 7
- [40] Wenhai Wang, Enze Xie, Xiang Li, Deng-Ping Fan, Kaitao Song, Ding Liang, Tong Lu, Ping Luo, and Ling Shao. Pyramid vision transformer: A versatile backbone for dense prediction without convolutions. In *Proceedings of the IEEE/CVF international conference on computer vision*, pages 568–578, 2021. 1
- [41] Enze Xie, Junsong Chen, Junyu Chen, Han Cai, Haotian Tang, Yujun Lin, Zhekai Zhang, Muyang Li, Ligeng Zhu, Yao Lu, et al. Sana: Efficient high-resolution text-to-image synthesis with linear diffusion transformers. In *The Thirteenth International Conference on Learning Representations*, 2025. 6
- [42] Tianzhu Ye, Li Dong, Yuqing Xia, Yutao Sun, Yi Zhu, Gao Huang, and Furu Wei. Differential transformer. In *The Thirteenth International Conference on Learning Representations*, 2025. 1, 3, 4, 6, 7
- [43] Yundong Zhang, Huiye Liu, and Qiang Hu. Transfuse: Fusing transformers and cnns for medical image segmentation. In *International conference on medical image computing and computer-assisted intervention*, pages 14–24. Springer, 2021. 7

Gated Differential Linear Attention: A Linear-Time Decoder for High-Fidelity Medical Segmentation

Supplementary Material

6. Preliminary

6.1. Multi-Head Softmax Attention

Let the input be $X \in \mathbb{R}^{N \times d_{\text{model}}}$, where N is the number of tokens (e.g., $N = \mathcal{HW}$ for a 2D grid) and d_{model} is the channel width. The softmax attention [37] operates with the following steps.

Input Linear Projections. The input X is linearly transformed into queries Q , keys K , and values $V \in \mathbb{R}^{d_{\text{model}} \times d_k}$ via learned weight matrices $W^Q, W^K, W^V \in \mathbb{R}^{d_{\text{model}} \times d_k}$,

$$Q = XW^Q, \quad K = XW^K, \quad V = XW^V. \quad (31)$$

Scaled Dot-Product (Softmax) Attention. The scaled dot-product attention (SDPA) is computed as

$$\text{Attention}(Q, K, V) = \text{softmax}\left(\frac{QK^\top}{\sqrt{d_k}}\right)V \in \mathbb{R}^{n \times d_k}, \quad (32)$$

where $QK^\top/\sqrt{d_k}$ represents the similarity matrix, and $\text{softmax}(\cdot)$ ensures non-negative weights that sum to 1 per query token.

Multi-Head Concatenation. In multi-head attention, in multi-head attention, the procedure is executed in parallel across h heads. Each head has its own projections $W_i^Q, W_i^K, W_i^V \in \mathbb{R}^{d_{\text{model}} \times d_h}$ for $i \in [1, h]$. For head $i \in \mathbb{R}^{d_{\text{model}} \times d_h}$, we compute

$$\text{head}_i = \text{Attention}(QW_i^Q, KW_i^K, VW_i^V). \quad (33)$$

Then, we concatenate the heads along the channel dimension yields

$$\text{MultiHead}(Q, K, V) = \text{Concat}(\text{head}_1, \dots, \text{head}_h). \quad (34)$$

Output Linear Projection. The concatenated multi-head output is linearly projected with a learnable matrix $W^O \in \mathbb{R}^{hd_h \times d_{\text{model}}}$,

$$O = \text{MultiHead}(Q, K, V)W^O. \quad (35)$$

7. Experiment

This section extends our Section 4 in the main paper by detailing the datasets, implementation details, evaluation metrics, followed by additional experimental results.

7.1. Dataset and Implementation Details

Synapse Multi-Organ. We follow the TransUNet protocol [8] on *Synapse* (30 CT scans), using 18 scans for training and 12 for validation. Training runs for 200 epochs with 10 warmup epochs, batch size 8, and AdamW [22] with learning rate 5×10^{-4} .

Automated Cardiac Diagnosis Challenge (ACDC). On *ACDC* [4] (100 cardiac MRI scans), we split 70/10/20 for train/val/test. Training uses 150 epochs with 10 warmup epochs, batch size 16, and AdamW with learning rate 5×10^{-4} .

Breast Ultrasound Images Dataset (BUSI). For *BUSI* [1], we adopt an 80/10/10 train/val/test split. Training uses 100 epochs with 10 warmup epochs, batch size 16, and AdamW with learning rate 5×10^{-4} .

HAM10000. For *HAM10000* [36] (10,015 dermoscopic images), we use a 70/10/20 train/val/test split. Training uses 150 epochs with 10 warmup epochs, batch size 16, and AdamW with learning rate 5×10^{-4} .

PH². On *PH²* [25] (200 images), the split is 80 train, 20 validation, and 100 test images. Training uses 100 epochs with 5 warmup epochs, batch size 16, and AdamW with learning rate 5×10^{-4} .

7.2. Evaluation Metrics

We report Dice score (DSC) on all datasets and additionally the 95th-percentile Hausdorff distance (HD95) on *Synapse*. Metrics are computed per structure and then averaged.

Dice Score (DSC). For binary masks, let X be the model prediction and Y the ground truth. The Dice score is

$$\text{DSC}(X, Y) = \frac{2|X \cap Y|}{|X| + |Y|}. \quad (36)$$

95% Hausdorff Distance (HD95). Let $d(\cdot, \cdot)$ denote the Euclidean distance and let X and Y be the (boundary) point sets of the prediction and ground truth, respectively. The directed Hausdorff distance is

$$h(X, Y) = \max_{x \in X} \min_{y \in Y} d(x, y), \quad (37)$$

and the (symmetric) Hausdorff distance is

$$H(X, Y) = \max\{h(X, Y), h(Y, X)\}. \quad (38)$$

The 95th-percentile variant replaces the outer maximum with the 95th percentile of one-sided distances:

$$\text{HD}_{95}(X, Y) = \max\{\text{percentile}_{95}(\{\min_{y \in Y} d(x, y) : x \in X\}), \text{percentile}_{95}(\{\min_{x \in X} d(y, x) : y \in Y\})\}. \quad (39)$$

7.3. Results

In this section, we provide additional qualitative results from dermoscopy datasets and analysis of the attention in the proposed gated differential linear attention (GDLA).

7.3.1. Result Visualization

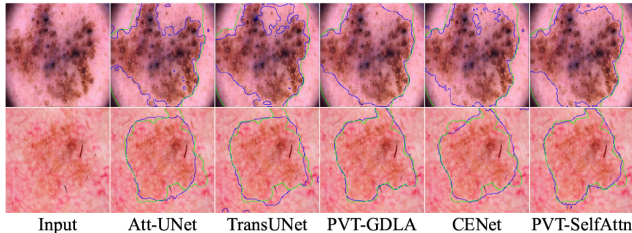


Figure 8. Visual comparison of the proposed method versus others on the Skin datasets. PH^2 (top) and $HAM10000$ (bottom). The blue and the green lines represent prediction and ground truth respectively.

Dermoscopic boundary quality. On the addition *skin* (dermoscopy) examples in Figure 8, PVT-GDLA traces lesion borders more tightly than Att-UNet, TransUNet, CENet, and PVT-SelfAttn. Across both large, irregular lesions (top row) and faint, low-contrast lesions with hair artifacts (bottom row), GDLA adheres to concave indentations and thin protrusions, avoids spurious “holes” inside the mask, and reduces background leakage along weak edges. Competing methods either over-smooth jagged boundaries, under-segment faint rims, or produce fragmented contours.

7.3.2. Attention Visualization

We further perform attention visualizations with differential attention and self-attention in Figure 9. Across decoder stages, the change-in-attention maps ($\|\Delta\text{attn}\|$) highlight consistent qualitative advantages of GDLA over linear, differential, and self attention. Linear attention (LA) produces broadly elevated, spatially diffuse updates, an indicator of attention dilution, while differential attention (DA) sharpens responses but still leaves spurious high-frequency activations in background regions. Self attention (SA) exhibits more localized updates than LA/DA, yet occasionally collapses onto a few dominant tokens (attention sink)

and incurs higher compute. In contrast, GDLA concentrates update energy along organ interiors and boundaries, suppresses background activations, and maintains balanced focus without collapse across scales. This pattern is stable from coarse to fine decoder stages and aligns with the observed Dice gains, suggesting that GDLA’s subtractive sharpening and lightweight gating improve boundary fidelity while preserving linear-time efficiency.

7.4. Ablation Study

7.4.1. Feed-Forward Network

We conduct experiments to evaluate the effectiveness of the three aforementioned feed-forward network (FFN) in Section 3.5 in our GDLA module. As shown in Table 5

Table 5. Effect of FFN design within GDLA. Comparison of three feed-forward variants, 2-layer MLP (4× expansion), SwiGLU, and Mix-FFN, evaluated by average Dice on *Synapse*, *ACDC*, and *HAM10000*.

FFN	Avg. Dice		
	Synapse	ACDC	HAM1000
2-layer MLP	84.73	92.33	94.84
SwiGLU	84.78	92.25	94.90
Mix-FFN	85.32	92.53	95.01

As shown in Table 5, Mix-FFN consistently yields the best Dice across all three datasets, improving over the 2-layer MLP by +0.59 on *Synapse*, +0.20 on *ACDC*, and +0.17 on *HAM10000*. Relative to SwiGLU, Mix-FFN gain +0.54 (*Synapse*), +0.28 (*ACDC*), and +0.11 (*HAM10000*). These consistent but modest gains indicate that depth-wise convolution local mixing complements GDLA’s global linear attention by strengthening short-range interactions and boundary detail, while keeping the decoder design parameter-efficient. In particular, the improvements on *Synapse* and *HAM10000*, which are sensitive to boundary fidelity, suggest that Mix-FFN is good at segmenting boundary regions.

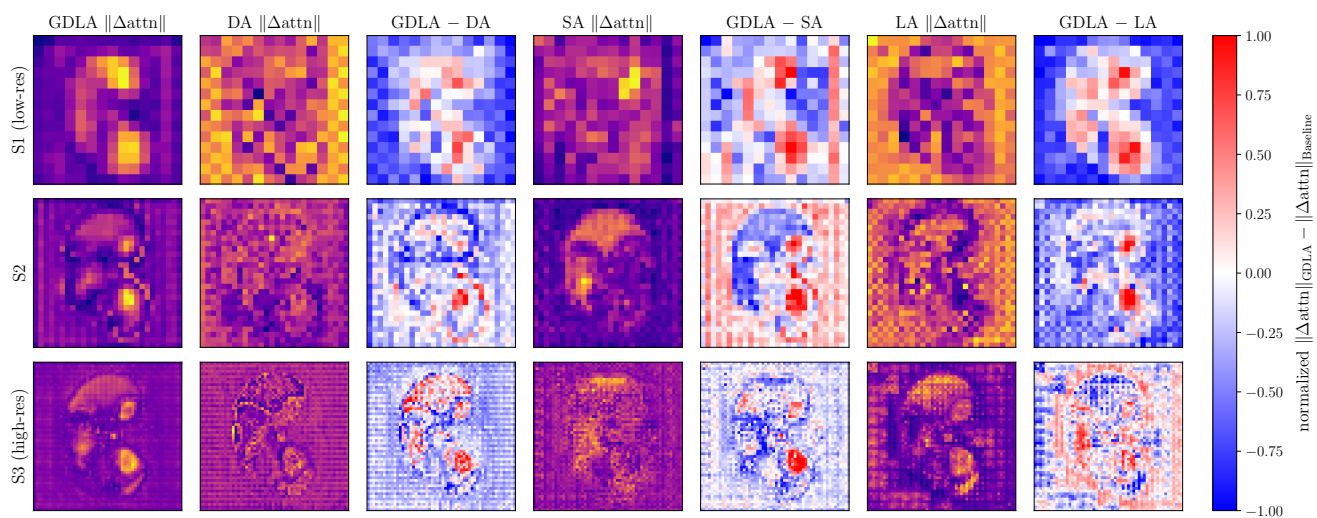


Figure 9. GDLA vs. baseline attentions on $\|\Delta\text{attn}\|$. Rows show decoder stages (S1–S3, coarse \rightarrow fine). Columns display per-method update magnitudes for GDLA, Differential Attention (DA), Self Attention (SA), and Linear Attention (LA), alongside normalized difference maps ($\|\Delta\text{attn}\|_{\text{GDLA}} - \|\Delta\text{attn}\|_{\text{baseline}}$).